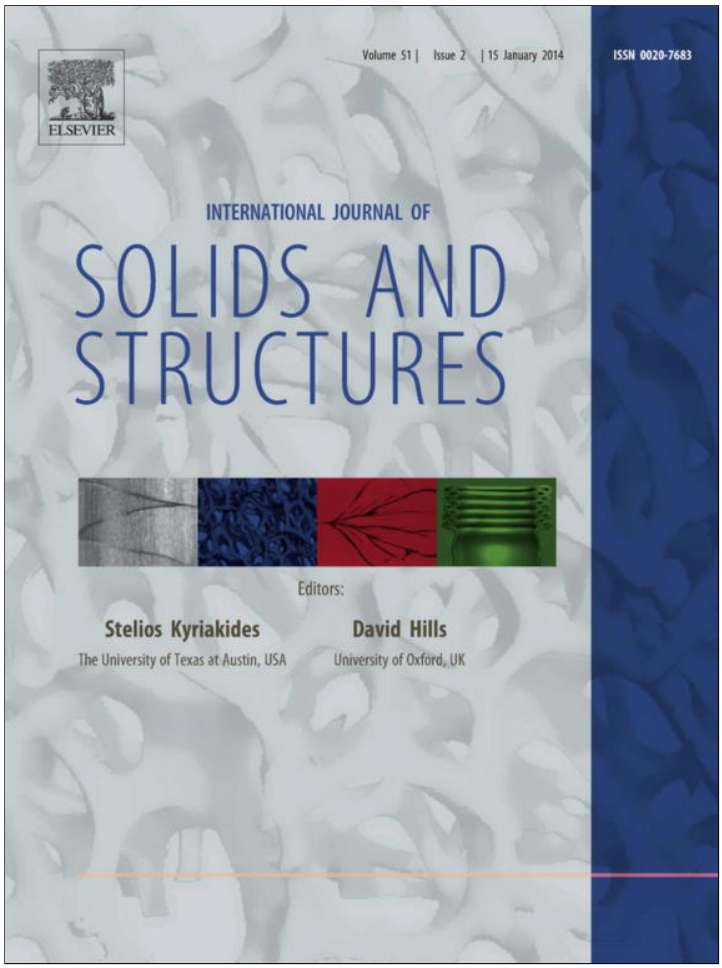

International Journal of Solids and Structures 51 (2014) 295–304

Contents lists available at ScienceDirect

International Journal of Solids and Structures

journal homepage: www.elsevier.com/locate/ijsolstr

Identification of orthotropic elastic constants using the Eigenfunction Virtual Fields Method

N. Nigamaa, S.J. Subramanian *

Department of Engineering Design, Indian Institute of Technology Madras, Chennai 600 036, India

ARTICLE INFO

Article history:
Received 22 January 2013
Received in revised form 10 September 2013
Available online 10 October 2013

Keywords:
Strain
Orthotropic elasticity
Full-field measurement
Principal components analysis
Virtual Fields Method
Eigenfunction
Inverse problem
Noise

ABSTRACT

The Virtual Fields Method (VFM – Pierron and Grediac, 2012), an inverse method based on the principle of virtual work (PVW), is being increasingly used to estimate mechanical properties of materials from full-field deformations obtained from techniques such as Digital Image Correlation, moiré and speckle interferometry and grid methods. By making specific choices for virtual fields (VFs) in PVW, one obtains a system of algebraic equations, which is then solved for the unknown material constants. Recently, a new variant of VFM, known as the Eigenfunction Virtual Fields Method (EVFM) has been proposed (Subramanian, 2013). In EVFM, principal components of the measured (i.e. true) strain fields are used to systematically generate VFs. We extend EVFM to orthotropic elastic materials in this work, and estimate the relevant material parameters from full-field strain data generated from a finite-element model of an unnotched Iosipescu test. Varying levels of Gaussian white noise are added to the synthetic strain data to evaluate the sensitivity of EVFM to input noise. It is observed that for low to moderate noise, the material properties estimated by the proposed method are relatively insensitive to noise. However, when noise levels are high, the proposed method yields large variance in some of the computed properties when compared to the state-of-the-art optimized piecewise continuous VFM (Toussaint et al., 2006; Pierron and Grediac, 2012). Some of the large variance in properties estimated from noisy data using EVFM is traced to the sensitivity of the third dominant eigenfunction and modifications to the proposed method to address this issue are suggested.

1. Introduction

Identification of material parameters from experimental measurements of kinematic variables, especially from full-field techniques such as Digital Image Correlation (DIC), moiré and speckle interferometry and grid methods, is an active area of research in experimental mechanics (Avril et al., 2008). One of these techniques that is increasingly being used is the Virtual Fields Method (VFM – Grediac, 1989; Pierron and Grediac, 2012), an inverse method based on the principle of virtual work (PVW – Malvern, 1977). In the context of infinitesimal deformations, if inertial effects and body forces are small enough to be neglected, PVW may be stated as

$$\int_V \boldsymbol{\sigma} : \boldsymbol{\varepsilon}^* \mathrm{d}V = \int_{S_T} \boldsymbol{t} \cdot \boldsymbol{u}^* \mathrm{d}A, \tag{1}$$

where V is the volume occupied by the solid of interest, S_T is the portion of the exterior surface of the solid where tractions are prescribed, $\boldsymbol{\sigma}$ is any statically admissible stress field, $\boldsymbol{t}$ is the (true) traction vector specified on S_T, $\boldsymbol{u}^*$ is any kinematically admissible virtual displacement field and $\boldsymbol{\varepsilon}^* = \frac{1}{2}\left(\nabla \boldsymbol{u}^* + \nabla \boldsymbol{u}^{*T}\right)$ is the virtual strain field obtained by differentiating the virtual displacement field $\boldsymbol{u}^*$ with respect to the current configuration (Malvern, 1977). In the literature, the left hand side of Eq. (1) is commonly referred to as the *internal virtual work* and the right hand side the *external virtual work*.

VFM was first used in the estimation of linear elastic material parameters, which is also the topic of interest in this article. A good review of methods for inverse computation of linear elastic properties is found in Avril and Pierron (2007). We focus attention on the plane-stress deformation of a homogeneous, orthotropic linear elastic material in this work. Thus, the stress tensor $\boldsymbol{\sigma}$ is related to the strain $\boldsymbol{\varepsilon}$ through a uniform fourth-order elasticity tensor $\boldsymbol{C}$:

$$\boldsymbol{\sigma} = \boldsymbol{C}\boldsymbol{\varepsilon} \tag{2}$$

Following Voigt notation, $(\sigma_{11}, \sigma_{22}, \sigma_{12}) \equiv (\sigma_1, \sigma_2, \sigma_6)$; $(\varepsilon_{11}, \varepsilon_{22}, 2\varepsilon_{12}) \equiv (\varepsilon_1, \varepsilon_2, \varepsilon_6)$, Eq. (1) may be written in indicial form as

$$C_{ij} \int_V \varepsilon_i \varepsilon_j^* \mathrm{d}V = \int_{S_T} t_i u_i^* \mathrm{d}A \tag{3}$$

In VFM, advantage is taken of current experimental techniques such as Digital Image Correlation, moiré and speckle interferometry and grid methods, which generate spatially dense measurements

* Corresponding author. Tel.: +91 9884966705.
E-mail address: shankar_sj@iitm.ac.in (S.J. Subramanian).

0020-7683/$ - see front matter © 2013 Elsevier Ltd. All rights reserved.
http://dx.doi.org/10.1016/j.ijsolstr.2013.09.021

of strain components ε_i over the area of interest. For each choice of virtual field, the integrals on the left hand side and right hand side of Eq. (3) are explicitly computed, generating one linear equation in the unknown material parameters. If N independent material constants $p_\alpha,\ (\alpha = 1,\ N)$, feature in $\boldsymbol{C}$, then these p_α are computed by generating a sufficient number of linear equations for the unknowns by employing several different virtual displacement fields $u^{*(k)},\ (k = 1,\ d),\ d \geqslant N$ and solving the resulting system of equations $\boldsymbol{PQ} = \boldsymbol{R}$. Details of application of VFM to estimation of constitutive parameters of various linear and non-linear material models are found in the recent book on VFM (Pierron and Grediac, 2012).

The choice of virtual fields plays a vital role in the successful computation of the materials parameters p_α. In the earliest works, the virtual fields were chosen based on intuition and trial-and-error (Grediac et al., 1999), but these were not guaranteed to yield independent equations for the unknown material parameters. For this reason, so-called 'special' virtual fields were defined (Grediac et al., 2002a) to yield fully decoupled equations for the unknowns. These fields were called special since they rendered the matrix of virtual work coefficients ($\boldsymbol{P}$) equal to the identity matrix. However, a large number of nuisance parameters are introduced to define the virtual fields in this approach, which becomes computationally expensive. While Grediac et al. (2002a) employed special virtual fields that were continuous over the entire domain of interest, piece-wise virtual fields with virtual nodal displacements akin to those commonly used in the finite-element method were introduced by Toussaint et al. (2006). Virtual fields have also been chosen to be those that are least sensitive to experimental noise; this was investigated for the case of virtual fields continuous over the whole domain by Avril et al. (2004), and later extended to the case of piecewise virtual fields by Avril and Pierron (2007).

A different way of generating virtual fields has been recently proposed in Subramanian (2013). This approach differs markedly from those presented in the literature in that the form of the virtual fields is not determined *a priori*. Rather, the virtual fields are determined from the measured displacement field; they are, in fact, based on the eigenfunctions of the measured strain fields and hence, this method is called the Eigenfunction Virtual Fields Method (EVFM). Since actual measured strain fields are used in the computations, EVFM provides a physically-based and systematic means of selecting virtual strain fields and solving the resulting VFM equations for the unknown material parameters. Another significant advantage of EVFM is that no nuisance parameters (as in the case of full-domain or piece-wise virtual fields) are introduced to define the virtual fields since the eigenfunctions are completely defined by the measured strain fields. The proposed choice of virtual fields also leads to enormous algebraic simplification compared to existing VFM approaches, resulting in a compact system of equations to be solved.

In Subramanian (2013), the efficacy of EVFM was demonstrated by computing the Young's modulus and Poisson's ratio of a homogeneous, isotropic, linear elastic material using simulated strain data from a uniaxial tension test. While this simple example adequately elucidates the sequence of steps involved in EVFM, the test itself is too simplistic when compared to real data obtained from full-field experimental techniques. In order to address this issue, in this work, we apply EVFM to simulated strain data obtained from the plane-stress deformation of a plate of homogeneous, orthotropic, linear elastic material subjected to unnotched Iosipescu bending. The strain fields obtained are inhomogeneous compared to the simple homogeneous strain fields in uniaxial tension, and therefore provide richer, and more challenging data for evaluating EVFM. Moreover, Gaussian white noise of various levels is also added to the strain data to mimic actual experimental data and to make the present study more relevant to practical implementation. Finally, the unnotched Iosipescu test is a standard problem for benchmarking VFM and data from finite-element simulations and experiments are provided in the VFM book (Pierron and Grediac, 2012), thus facilitating direct validation of the present approach.

The rest of this paper is organized as follows. Principal components of measured strain matrices form the basis of EVFM and in Section 2, a brief summary of principal component analysis (PCA) of strain fields is presented. In Section 3, the finite-element model used to generate the data used in the present study is described, followed by the EVFM formulation for orthotropic materials in Section 4. Then, in Section 5, the virtual fields used to generate the EVFM equations for the present problem are presented in detail. In Sections 6 and 7 respectively, the results of the present work are presented and discussed and the main conclusions of this work are summarized in Section 8.

2. Computation of eigenfunctions of strain fields

EVFM is built around eigenfunctions of the measured strain components ε_1, ε_2 and ε_6 and therefore, computation of these eigenfunctions is discussed before the method itself is presented. It is assumed that experimentally measured strains are available on an $(m+1)\times(n+1)$ grid. From the centroids of the cells of this grid, a new grid of $m \times n$ points is obtained and the three strain components are generated on this new grid by simple averaging of the four surrounding values on the original grid. These values are stored in the three $m \times n$ matrices $\boldsymbol{E}_1,\ \boldsymbol{E}_2$, and $\boldsymbol{E}_6$ respectively. This averaging operation is introduced merely to simplify the algebra that appears later in this article, and is not essential to the efficacy of the method. Although this operation does introduce interpolation error into the original data, the grid over which full-field data is obtained is typically fine enough to make such interpolation errors insignificant.

From the generated strain component grids, two augmented matrices $\boldsymbol{E}^r$ and $\boldsymbol{E}^c$ of sizes $3m \times n$ and $m \times 3n$ respectively are formed as follows:

$$\boldsymbol{E^r} = \begin{bmatrix} \boldsymbol{E}_1 \\ \boldsymbol{E}_2 \\ \boldsymbol{E}_6 \end{bmatrix};\quad \boldsymbol{E^c} = [\,\boldsymbol{E}_1\boldsymbol{E}_2\boldsymbol{E}_6\,] \tag{4}$$

In this work, principal component analysis (PCA, Jolliffe, 2002) is used to investigate $\boldsymbol{E}^r$ and $\boldsymbol{E}^c$. Specifically, we use uncentred PCA (Noy-Meir, 1973; Cadima and Jolliffe, 2009) and obtain the eigenfunctions of $\boldsymbol{E}^r$ and $\boldsymbol{E}^c$ by performing Singular Value Decomposition (SVD), from which the following decompositions follow:

$$\begin{aligned} \boldsymbol{E}^r_{(3m\times n)} &= \boldsymbol{L}^r_{(3m\times 3m)}\boldsymbol{S}^r_{(3m\times n)}(\boldsymbol{R}^r)^T_{(n\times n)};\\ \boldsymbol{E}^c_{(m\times 3n)} &= \boldsymbol{L}^c_{(m\times m)}\boldsymbol{S}^c_{(m\times 3n)}(\boldsymbol{R}^c)^T_{(3n\times 3n)}, \end{aligned} \tag{5}$$

where

- the columns of $\boldsymbol{L}^r$ and $\boldsymbol{L}^c$ contain the *left singular vectors* of $\boldsymbol{E}^r$ and $\boldsymbol{E}^c$ respectively (i.e. the eigenvectors of $\boldsymbol{E}^r(\boldsymbol{E}^r)^T$ and $\boldsymbol{E}^c(\boldsymbol{E}^c)^T$);
- $\boldsymbol{S}^r$ and $\boldsymbol{S}^l$ are diagonal matrices that contain the *singular values* of $\boldsymbol{E}^r$ and $\boldsymbol{E}^c$;
- the columns of $\boldsymbol{R}^r$ and $\boldsymbol{R}^c$ contain the *right singular vectors* of $\boldsymbol{E}^r$ and $\boldsymbol{E}^c$ respectively (i.e. the eigenvectors of $(\boldsymbol{E}^r)^T\boldsymbol{E}^r$ and $(\boldsymbol{E}^c)^T\boldsymbol{E}^c$).

A significant benefit of this decomposition is that each set of singular vectors forms a complete orthonormal basis; thus, the right singular vectors form an orthonormal basis for the row space of each augmented matrix, while the left singular vectors form an orthonormal basis for the column space Strang (2006).

Let us denote by $\boldsymbol{r}$ the right singular vectors of $\boldsymbol{E}^r$ and by $\boldsymbol{l}$ the left singular vectors of $\boldsymbol{E}^c$, of length n and m respectively. It is also

assumed that the singular values of $\boldsymbol{E}^r$ and $\boldsymbol{E}^c$ are arranged in decreasing order, as is customary. Then, the number of principal singular vectors for each augmented matrix may be obtained (Jolliffe, 2002; Grama and Subramanian, 2013) by identifying the knee in the respective logarithmic plots of singular values (LSV). This technique is known as the 'scree-plot' technique in the PCA literature (Jolliffe, 2002), and consists of identifying a point on the LSV plot where it exhibits a sharp knee and becomes more or less horizontal. Several applications of this technique are shown in Section 6 of this manuscript. The principal left and right singular vectors of each augmented matrix show the dominant spatial patterns in each composite strain field along the X_1- and X_2-directions respectively and the contribution of the ith pattern to each matrix is reflected in the magnitude of the corresponding singular value λ_i Grama and Subramanian (2013).

Since the left and right singular vectors form an orthonormal basis for column and row spaces of the composite matrices respectively, the columns and rows of the strain matrices $\boldsymbol{E}_1, \boldsymbol{E}_2$, and $\boldsymbol{E}_3$ may be expanded in terms of these eigenfunctions.[1] It is frequently found that full-field strain data are highly redundant and only a small number $p \ll \min(m,n)$ eigenfunctions are *dominant*. Therefore, it is sufficient to reconstruct the strain matrices in terms of the p-dimensional subspace of the row and column spaces spanned by these p dominant left and right eigenfunctions respectively. If $\widetilde{\boldsymbol{E}}_1^r$ is the matrix of strain values ε_1 reconstructed using the p right eigenfunctions of $\boldsymbol{E}^r$, then

$$\widetilde{\boldsymbol{E}}_1^r = \widetilde{\boldsymbol{A}}_1^r (\widetilde{\boldsymbol{R}}^r)^T = \boldsymbol{E}_1 \widetilde{\boldsymbol{R}}^r (\widetilde{\boldsymbol{R}}^r)^T, \tag{6}$$

where $\widetilde{\boldsymbol{R}}^r$ is the $n \times p$ matrix whose columns contain the p dominant right eigenfunctions of $\boldsymbol{E}^r$ and $\widetilde{\boldsymbol{A}}_1^r = \boldsymbol{E}_1 \widetilde{\boldsymbol{R}}^r$ is an $m \times p$ matrix of components of the rows of $\boldsymbol{E}_1$ along the columns of $\widetilde{\boldsymbol{R}}^r$. Thus, the kth row $(\widetilde{\boldsymbol{E}}_1^r)^{(k,\bullet)}$ of $\widetilde{\boldsymbol{E}}_1^r$ may be expressed as

$$(\widetilde{\boldsymbol{E}}_1^r)^{(k,\bullet)} = (\widetilde{\boldsymbol{A}}_1^r)^{(k,\bullet)} (\widetilde{\boldsymbol{R}}^r)^T \tag{7}$$

Similarly, $\widetilde{\boldsymbol{E}}_1^c$, the matrix of ε_1 values reconstructed from the p dominant left eigenfunctions of $\boldsymbol{E}^c$ is written as

$$\widetilde{\boldsymbol{E}}_1^c = \widetilde{\boldsymbol{L}}^c \widetilde{\boldsymbol{A}}_1^c = \widetilde{\boldsymbol{L}}^c (\widetilde{\boldsymbol{L}}^c)^T \boldsymbol{E}_1 \tag{8}$$

with $\widetilde{\boldsymbol{L}}^c$ being the $m \times p$ matrix whose columns contain the p dominant left eigenfunctions of $\boldsymbol{E}^c$ and $\widetilde{\boldsymbol{A}}_1^c = (\widetilde{\boldsymbol{L}}^c)^T \boldsymbol{E}_1$ a $p \times n$ matrix of components of the columns of $\boldsymbol{E}_1$ along the columns of $\widetilde{\boldsymbol{L}}^c$. Similar reconstructions are defined for the other two strain component matrices.

3. Finite element analysis

In this work, the recently introduced technique of EVFM (Subramanian, 2013) is extended to the identification of constitutive parameters of orthotropic, linear elastic materials. Although the principle of virtual work Eq. (1) involves integrals over the volume, practical applications of VFM call for adaptation of this equation to in-plane deformations (Pierron and Grediac, 2012). Under plane-stress conditions, which are commonly assumed to prevail in VFM applications, and infinitesimal deformations, stresses are related to strains in orthotropic, linear elastic materials through the relation:

$$\begin{Bmatrix} \sigma_1 \\ \sigma_2 \\ \sigma_6 \end{Bmatrix} = \begin{bmatrix} Q_{11} & Q_{12} & 0 \\ Q_{12} & Q_{22} & 0 \\ 0 & 0 & Q_{66} \end{bmatrix} \begin{Bmatrix} \varepsilon_1 \\ \varepsilon_2 \\ \varepsilon_6 \end{Bmatrix} \tag{9}$$

[1] In the rest of this work, we will refer to the left and right singular vectors collectively as eigenfunctions.

where Q_{11}, Q_{12}, Q_{22} and Q_{66} are the orthotropic material parameters to be evaluated using VFM (Pierron and Grediac, 2000; Grediac et al., 2002b; Avril et al., 2004; Pierron et al., 2007; Pierron and Grediac, 2012).

We use the well-documented unnotched Iosipescu test (see Pierron and Grediac, 2012, Chap. 13) to demonstrate the application of EVFM to orthotropic elastic materials. In this test, a thin rectangular specimen of thickness h is asymmetrically clamped as shown in Fig. 1. The supports at the left are held fixed, while those at the right are displaced rigidly. Under these boundary conditions, the free span in the centre of the specimen undergoes a combination of bending and shear, the relative contributions of each of which may be varied by changing the geometry and/or loading conditions of the specimen. All four of the in-plane orthotropic elastic constants influence the resulting deformation and VFM can be used to compute these if the strain fields in the specimen are available.

Since the primary objective of this work is to demonstrate the applicability of EVFM for the material property identification of in-plane orthotropic constants, we generate our strain fields from a finite-element (FE) solution to the test configuration described above. This approach, which has previously been adopted by Pierron and Grediac and their co-workers, also provides us the opportunity to compare our results directly with their published data. We generate our strain fields using the same geometry and material parameters as listed in Section 13.1.3 of Pierron and Grediac (2012) and these are listed in Table 1. Further, we discretize the geometry with 4-noded bilinear two-dimensional plane-stress elements using full integration. Pierron and Grediac (2012) employed a mesh with 50×75 elements in the mid-section of the plate; however, we use a mesh that has four times this density since our analysis indicates that a finer mesh is required to obtain mesh-insensitive results. The applied displacements are adjusted to yield the same total applied force of 702 N as in Pierron and Grediac (2012). The strain fields obtained from FEA are as shown in Fig. 2 and the three strain components computed at the centroids of the elements are stored for EVFM analysis. Although the FE analysis yields the reaction forces at all nodes on the surfaces AB, CD, EF and GH, only the total force is invoked in the EVFM analysis in order to faithfully simulate an experimental measurement in which the distribution of tractions is typically unknown.

4. EVFM for orthotropic material property identification

Substituting the orthotropic constitutive Eq. (9) in Eq. (1), we obtain

$$\int_V (Q_{11}\varepsilon_1 + Q_{12}\varepsilon_2)\varepsilon_1^* \mathrm{dV} + \int_V (Q_{12}\varepsilon_1 + Q_{22}\varepsilon_2)\varepsilon_2^* \mathrm{dV} + \int_V (Q_{66}\varepsilon_6)\varepsilon_6^* \mathrm{dV} = \int_{S_T} (t_1 u_1^* + t_2 u_2^*) \mathrm{dS} \tag{10}$$

In VFM, a system of linear equations in the unknown Q_{ij} is obtained by substituting several virtual strain and displacement fields into

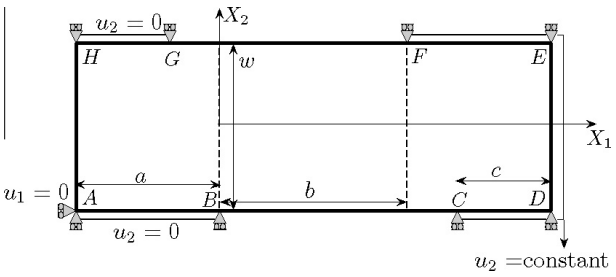

Fig. 1. Geometry and boundary conditions for the unnotched Iosipescu test following Pierron and Grediac (2012).

Table 1
Values of material and geometry parameters used in FE model, following Pierron and Grediac (2012).

a (mm)	b (mm)	c (mm)	w (mm)	h (mm)	Q_{11} (GPa)	Q_{22} (GPa)	Q_{12} (GPa)	Q_{66} (GPa)
23	30	15	20	2.3	41	10.3	3.1	4

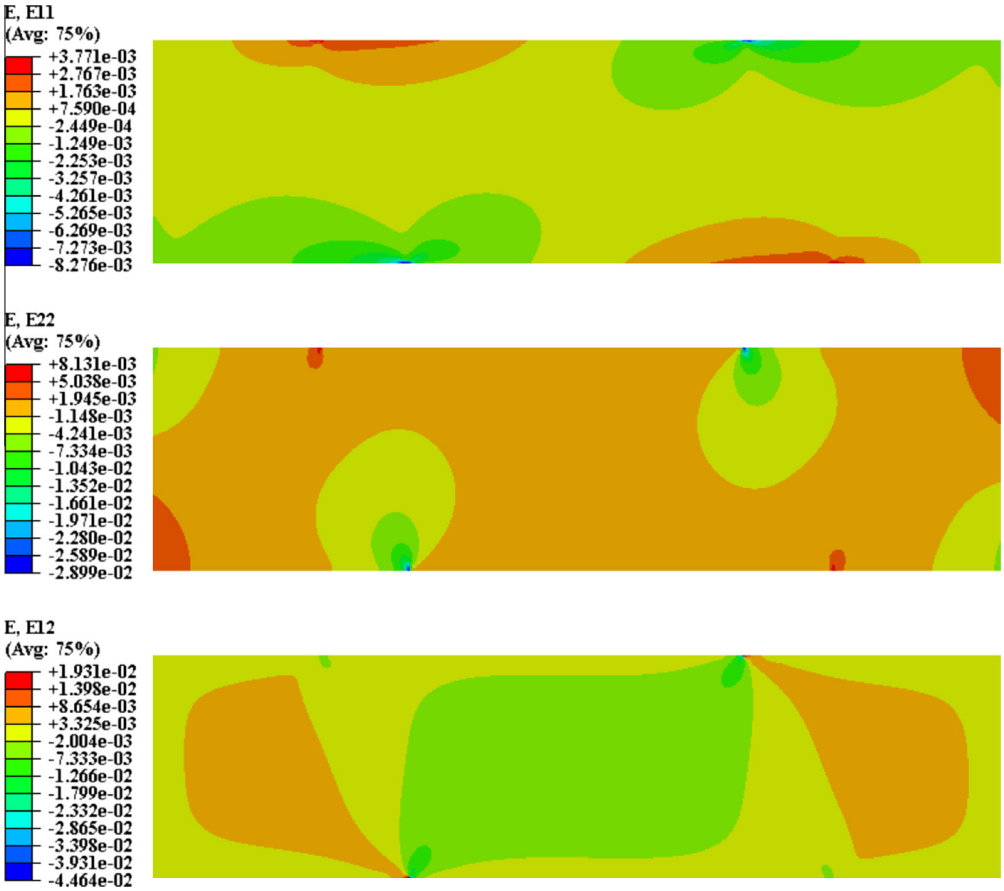

Fig. 2. Strain fields obtained from finite element analysis, showing concentrations near the support edges.

Eq. (10) and computing the resulting integrals. The virtual strain fields are constructed directly from the eigenfunctions of the true strain fields and this idea forms the basis of the Eigenfunction Virtual Fields Method (VFM – Subramanian, 2013). In this section, we describe in detail the choice of virtual fields and the structure of the resulting equations.

Kinematically admissible virtual displacement fields must vanish on parts of the boundary where displacements are prescribed. In the current problem, there are four segments on the exterior boundary where displacements are specified and requiring the virtual displacement fields to vanish on these segments poses a restriction on the choice of virtual fields. We circumvent this issue by choosing two sub-domains of the plate such that the entire outer surface of each of these domains contains no regions of prescribed displacements, thus freeing the virtual displacements of any boundary conditions. The first of these, denoted by V_A and shown in Fig. 3, is taken from the mid-span and extends vertically through the entire height of the specimen. However, a narrow vertical strip extending from $X_1 = a$ to $X_1 = a + \Delta_A$ and another from $X_1 = a + b - \Delta_A$ to $X_1 = a + b$ is excluded from V_A so as to exclude any prescribed displacements from this domain. Likewise, a second sub-domain, V_B (Fig. 3), is constructed by excluding narrow horizontal strips of width Δ_B at the top and bottom of the plate; thus, the segments AB, CD, EF and GH which contain prescribed displacements are excluded from V_B.

Once the sub-domains are defined, the centroidal strain values from the elements comprising these sub-domains are assembled into the augmented strain matrices. As explained in Grama and Subramanian (2013), the logarithm of singular values (LSV) plots of these augmented strain matrices are inspected to identify the dominant singular values. For the problem at hand, sub-domains A and B yield 28 dominant singular values. The first four dominant left eigenfunctions of $\mathbf{E}^{\mathbf{c}}$ for sub-domain A are shown in Fig. 4 for illustration.

The central feature of EVFM is the use of eigenfunctions of the strain matrices to generate the virtual strain fields. These eigenfunctions, being generated through SVD of the augmented strain matrices, are discrete vectors, while the virtual strain fields occurring in the PVW Eq. (10) are continuous over the domain of interest. Therefore, it is necessary to define continuous analogues of the strain eigenfunctions before they can be used in EVFM. In this work, we define the following piecewise-constant versions of a generic right eigenfunction $\boldsymbol{r}$ and left eigenfunction $\boldsymbol{l}$ respectively:

$$f_n(X_1;\boldsymbol{r}) = \sum_{k=1}^{n} N^k(X_1) r^k; \quad N^k(X_1) = \begin{cases} 1, & \text{if } (X_1)^k - \frac{\Delta X_1}{2} < X_1 < (X_1)^k + \frac{\Delta X_1}{2} \\ 0, & \text{otherwise} \end{cases}, \tag{11}$$

$$f_m(X_2;\ \boldsymbol{l}) = \sum_{k=1}^{m} N^k(X_2) l^k; \quad N^k(X_2) = \begin{cases} 1, & \text{if } (X_2)^k - \frac{\Delta X_2}{2} < X_2 < (X_2)^k + \frac{\Delta X_2}{2} \\ 0, & \text{otherwise} \end{cases}, \tag{12}$$

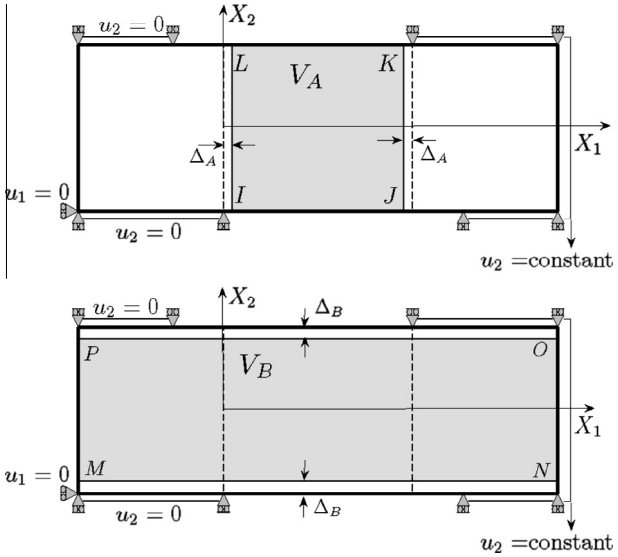

Fig. 3. Sub-domains A (shaded region, top) and B (shaded region, bottom) used to generate EVFM equations, shown with their respective coordinate systems.

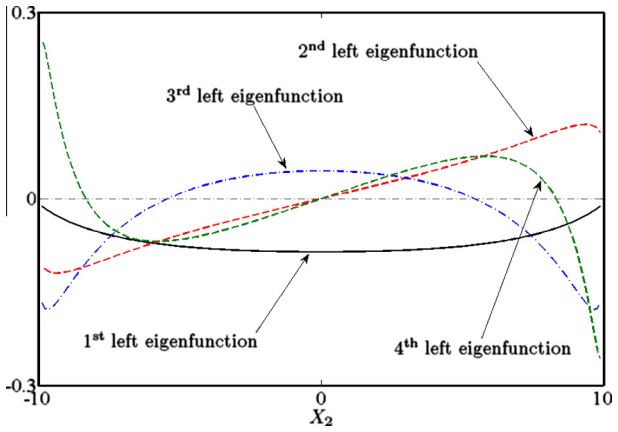

Fig. 4. The first four left eigenfunctions of $\mathbf{E}^c$ for sub-domain B.

where ΔX_1 and ΔX_2 are the grid sizes along the X_1 and X_2 directions, $(X_1)^k$ and $(X_2)^k$ are the X_1 and X_2 values at the kth grid location, and r^k and l^k are the kth component of the right and left eigenfunctions $\boldsymbol{r}$ and $\boldsymbol{l}$ respectively. The integrals of these piecewise-constant functions, which will be required to evaluate the virtual work integrals, are defined as

$$P_n(X_1;\ \boldsymbol{r}_i) = \int_0^{X_1} f_n(X_1;\ \boldsymbol{r}_i)ds; \quad P_m(X_2;\ \boldsymbol{l}_i) = \int_0^{X_1} f_m(X_2;\ \boldsymbol{l}_i)ds, \quad (13)$$

where $\boldsymbol{r}_i$ and $\boldsymbol{l}_i$ are the right eigenvector of $\boldsymbol{E}^r$ and the ith left eigenvector of $\boldsymbol{E}^c$ respectively.

Due to the orthonormality of the left and right eigenfunctions (Strang, 2006), one obtains the result

$$\begin{aligned} &\int_0^{L_1} f_n(X_1;\ \boldsymbol{r}_i) f_n(X_1;\ \boldsymbol{r}_j)\mathrm{d}X_1 = \delta_{ij}\Delta X_1 \\ &\int_0^{L_2} f_m(X_2;\ \boldsymbol{l}_i) f_m(X_2;\ \boldsymbol{l}_j)\mathrm{d}X_2 = \delta_{ij}\Delta X_2 \end{aligned} \quad (14)$$

where δ_{ij} is the Kronecker delta, equal to 1 if $i = j$ and 0 otherwise.

The strain component fields ε_1, ε_2 and ε_6 are expressed as linear combinations of the piecewise-continuous p dominant

- right eigenfunctions

$$\begin{aligned} \varepsilon_1(X_1,(X_2)^k) &= \sum_{t=1}^{p} (\widetilde{\mathbf{A}}_1^r)^{(k,t)} f_n(X_1;\ \boldsymbol{r}_t) \\ \varepsilon_2(X_1,(X_2)^k) &= \sum_{t=1}^{p} (\widetilde{\mathbf{A}}_2^r)^{(k,t)} f_n(X_1;\ \boldsymbol{r}_t) \\ \varepsilon_6(X_1,(X_2)^k) &= \sum_{t=1}^{p} (\widetilde{\mathbf{A}}_6^r)^{(k,t)} f_n(X_1;\ \boldsymbol{r}_t) \end{aligned} \quad (15)$$

- or left eigenfunctions:

$$\begin{aligned} \varepsilon_1((X_1)^k,X_2) &= \sum_{t=1}^{p} (\widetilde{\mathbf{A}}_1^c)^{(t,k)} f_m(X_2;\ \boldsymbol{l}_t) \\ \varepsilon_2((X_1)^k,X_2) &= \sum_{t=1}^{p} (\widetilde{\mathbf{A}}_2^c)^{(t,k)} f_m(X_2;\ \boldsymbol{l}_t) \\ \varepsilon_6((X_1)^k,X_2) &= \sum_{t=1}^{p} (\widetilde{\mathbf{A}}_6^c)^{(t,k)} f_m(X_2;\ \boldsymbol{l}_t) \end{aligned} \quad (16)$$

5. Construction of Virtual Fields

In this section, we describe how the four virtual fields required to generate the four equations for Q_{11}, Q_{22}, Q_{12} and Q_{66} are constructed. First, we work with the strain fields in sub-domain A, whose exterior surface consists of the four segments IJ, JK, KL and LI. Traction boundary conditions on these segments are as follows and equal and opposite forces of 702 N act on the faces IL and JK (Fig. 5):

$$S_T: \begin{cases} IJ: & t_1 = 0 & t_2 = 0 \\ JK: & t_1 \neq 0; & t_2 \neq 0; \quad \int_{JK} t_1 \mathrm{d}S = 0; \quad \int_{JK} t_2 \mathrm{d}S = -F_A \\ KL: & t_1 = 0 & t_2 = 0 \\ LI: & t_1 \neq 0; & t_2 \neq 0; \quad \int_{LI} t_1 \mathrm{d}S = 0; \quad \int_{LI} t_2 \mathrm{d}S = F_A \end{cases} \quad (17)$$

Over this sub-domain, we generate two virtual fields based on the most dominant right eigenfunction $\boldsymbol{r}_1$ of the row-augmented strain matrix $\mathbf{E}^{\mathbf{r}}$.

- Virtual Field 1 (VF1):

$$\begin{aligned} &u_1^* = 0; \quad u_2^* = P_n(X_1;\ \boldsymbol{r}_1) \\ &\varepsilon_1^* = 0; \quad \varepsilon_2^* = 0; \quad \varepsilon_6^* = f_n(X_1;\ \boldsymbol{r}_1), \end{aligned} \quad (18)$$

- Virtual Field 2 (VF2):

$$\begin{aligned} &u_1^* = P_n(X_1;\ \boldsymbol{r}_1); \quad u_2^* = 0 \\ &\varepsilon_1^* = f_n(X_1;\ \boldsymbol{r}_1); \quad \varepsilon_2^* = 0; \quad \varepsilon_6^* = 0; \end{aligned} \quad (19)$$

VF1 represents a shear deformation while VF2 represents a non-uniform elongation along the X_1 direction, as illustrated in Fig. 6.

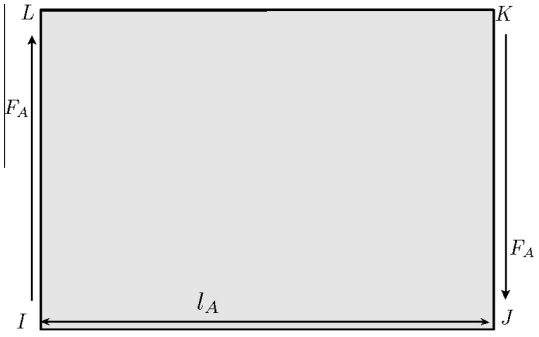

Fig. 5. Net force on the exterior surfaces of sub-domain A.

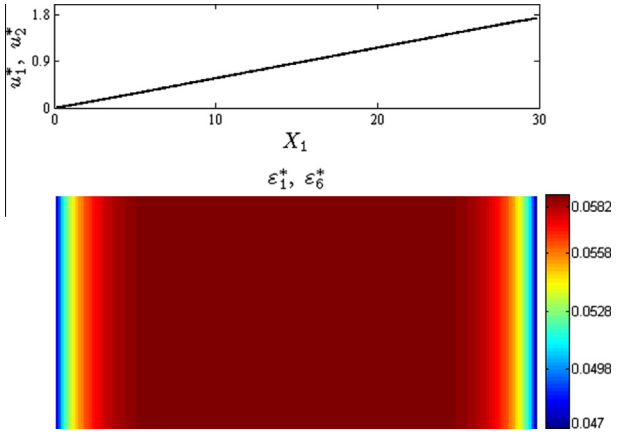

Fig. 6. VF1 and VF2 are both based on the first right eigenfunction $\boldsymbol{r}_1$. The contour plot represents the variation of ε_6^* (VF1) and ε_1^* (VF2) over V_A while the line-plot on the top shows the variation of virtual strain u_2^* (VF1) and u_1^* (VF2) along X_1.

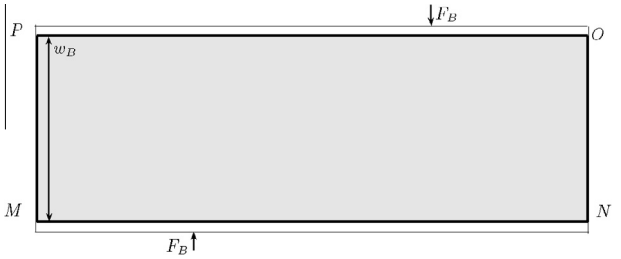

Fig. 7. sub-domain B is acted on by a pair of equal and opposite vertical forces F_B.

The third and fourth virtual fields are constructed using the first and second dominant left eigenfunctions of the column-augmented strain matrix $\mathbf{E}^{\mathbf{c}}$ for sub-domain B. The traction boundary conditions over the exterior of this sub-domain are as follows and are indicated schematically in Fig. 7:

$$S_T:\begin{cases} MN: & t_1\neq 0; \quad t_2\neq 0; \quad \int_{MN} t_1 dS = 0; \quad \int_{MN} t_2 dS = F_B \\ NO: & t_1 = 0; \quad t_2 = 0; \\ OP: & t_1\neq 0; \quad t_2\neq 0; \quad \int_{OP} t_1 dS = 0; \quad \int_{OP} t_2 dS = -F_B \\ PM: & t_1 = 0; \quad t_2 = 0; \end{cases} \tag{20}$$

Virtual Field 3 and Virtual Field 4 are respectively constructed from the first and third dominant left eigenfunctions of $\mathbf{E}^{\mathbf{c}}$:

- Virtual Fields 3 and 4 (VF3, VF4):

$$\begin{aligned} &(i=1,3)\quad u_1^*=0; \quad u_2^*=P_m(X_2;\ \boldsymbol{l}_i) \\ &\varepsilon_1^*=0; \quad \varepsilon_2^*=f_m(X_2;\ \boldsymbol{l}_i); \quad \varepsilon_6^*=0 \end{aligned} \tag{21}$$

Although the second dominant left eigenfunction yields a legitimate eigenfunction, for the present data, it yields virtual work integrals that vanish and therefore is not useful. Hence, the third dominant left eigenfunction is used instead. Both VF3 and VF4 represent a non-uniform vertical contraction, which is independent of X_1. The virtual strain contours corresponding to these virtual strain fields are shown in Fig. 8.

5.1. EVFM equations

Substitution of the virtual field expressions Eqs. 18, 19 and 21the tractions boundary conditions as given in Eqs. (17) and (20) into the principle of virtual work Eq. (10) leads to the following four equations:

$$\int_V (Q_{66}\varepsilon_6) f_n(X_1;\ \boldsymbol{r}_1) dV = -F_A P_n(l_A;\ \boldsymbol{r}_1) \tag{22}$$

$$\int_V (Q_{11}\varepsilon_1 + Q_{12}\varepsilon_2) f_n(X_1;\ \boldsymbol{r}_1) dV = 0 \tag{23}$$

$$\int_V (Q_{12}\varepsilon_1 + Q_{22}\varepsilon_2) f_m(X_2;\ \boldsymbol{l}_1) dV = -F_B P_m(w_B;\ \boldsymbol{l}_1) \tag{24}$$

$$\int_V (Q_{12}\varepsilon_1 + Q_{22}\varepsilon_2) f_m(X_2;\ \boldsymbol{l}_3) dV = -F_B P_m(w_B;\ \boldsymbol{l}_3) \tag{25}$$

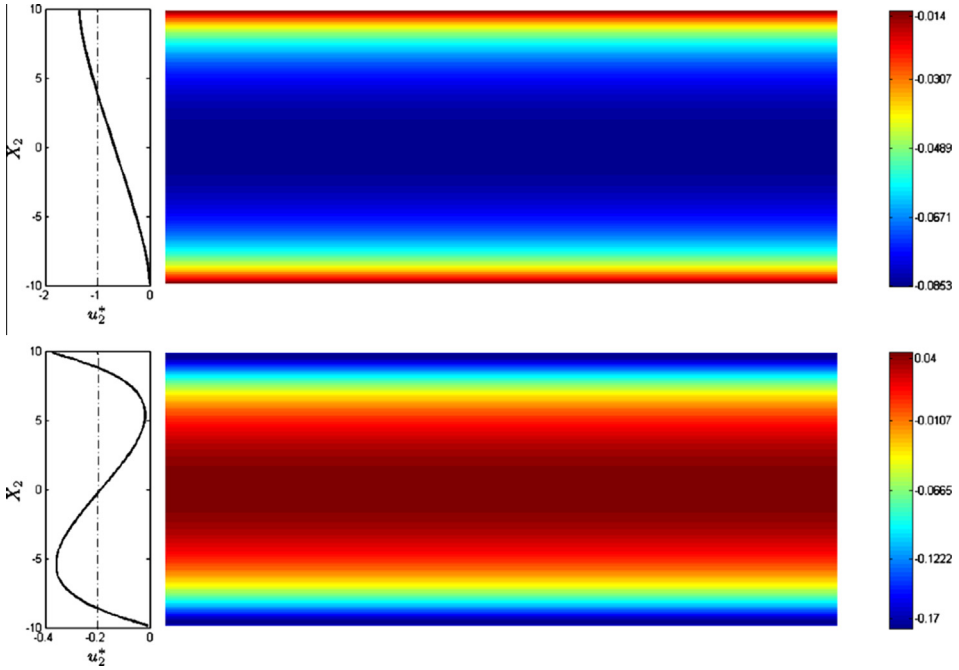

Fig. 8. VF3 (top) and VF4 (bottom) represent an X_1-independent non-uniform elongation along the X_2 direction. The contour plots show the variation of ε_2^* over V_B while the line-plots on the left show the variation of virtual strain u_2^* with X_2.

The first two of these equations contain virtual fields that do not vary across rows, while the last two contain virtual fields that do not vary along columns. To proceed further, we expand the true strain $\varepsilon_1, \varepsilon_2$ and ε_6 in terms of the right (for Eqs. (22) and (23)) or left (for Eqs. (24) and (25)) eigenfunction bases as expressed in Eqs. (15) and (16). Next, we evaluate the area integrals in Eqs. (22) and (23) by dividing them into horizontal strips (as described in Subramanian, 2013) while the integrals in Eqs. (24) and (25) are evaluated over vertical strips. This approach allows us to use the orthogonality of eigenfunctions (Eq. (14)) and obtain the following simple system of equations for the unknown material parameters:

$$\begin{bmatrix} 0 & 0 & 0 & A_{14} \\ A_{21} & 0 & A_{23} & 0 \\ 0 & A_{32} & A_{33} & 0 \\ 0 & A_{42} & A_{43} & 0 \end{bmatrix} \begin{Bmatrix} Q_{11} \\ Q_{22} \\ Q_{12} \\ Q_{66} \end{Bmatrix} = \begin{Bmatrix} B_1 \\ B_2 \\ B_3 \\ B_4 \end{Bmatrix} \tag{26}$$

or more compactly in the form $\mathbf{AQ} = \mathbf{B}$, where $\mathbf{A}$ is a (4×4) matrix with the following entries

$$\begin{aligned} A_{14} &= h\Delta X_1 \Delta X_2 \left[\sum_{k=1}^{m} \left(\widetilde{\mathbf{A}}_6^r\right)^{(k,1)}\right] \\ A_{21} &= h\Delta X_1 \Delta X_2 \left[\sum_{k=1}^{m} \left(\widetilde{\mathbf{A}}_1^r\right)^{(k,1)}\right]; \quad A_{23} = h\Delta X_1 \Delta X_2 \left[\sum_{k=1}^{m} \left(\widetilde{\mathbf{A}}_2^r\right)^{(k,1)}\right] \\ A_{32} &= h\Delta X_1 \Delta X_2 \left[\sum_{k=1}^{n} \left(\widetilde{\mathbf{A}}_1^c\right)^{(1,k)}\right]; \quad A_{33} = h\Delta X_1 \Delta X_2 \left[\sum_{k=1}^{n} \left(\widetilde{\mathbf{A}}_2^c\right)^{(1,k)}\right] \\ A_{42} &= h\Delta X_1 \Delta X_2 \left[\sum_{k=1}^{n} \left(\widetilde{\mathbf{A}}_1^c\right)^{(3,k)}\right]; \quad A_{43} = h\Delta X_1 \Delta X_2 \left[\sum_{k=1}^{n} \left(\widetilde{\mathbf{A}}_2^c\right)^{(3,k)}\right] \end{aligned} \tag{27}$$

and $\mathbf{B}$ is a 4×1 matrix with the following entries

$$\begin{aligned} B_1 &= -F_A \Delta X_1 \left[\sum_{t=1}^{n} r_1^t\right]; \quad B_2 = 0; \\ B_3 &= -F_B \Delta X_2 \left[\sum_{t=1}^{m} l_1^t\right]; \quad B_4 = -F_B \Delta X_2 \left[\sum_{t=1}^{m} l_3^t\right]; \end{aligned} \tag{28}$$

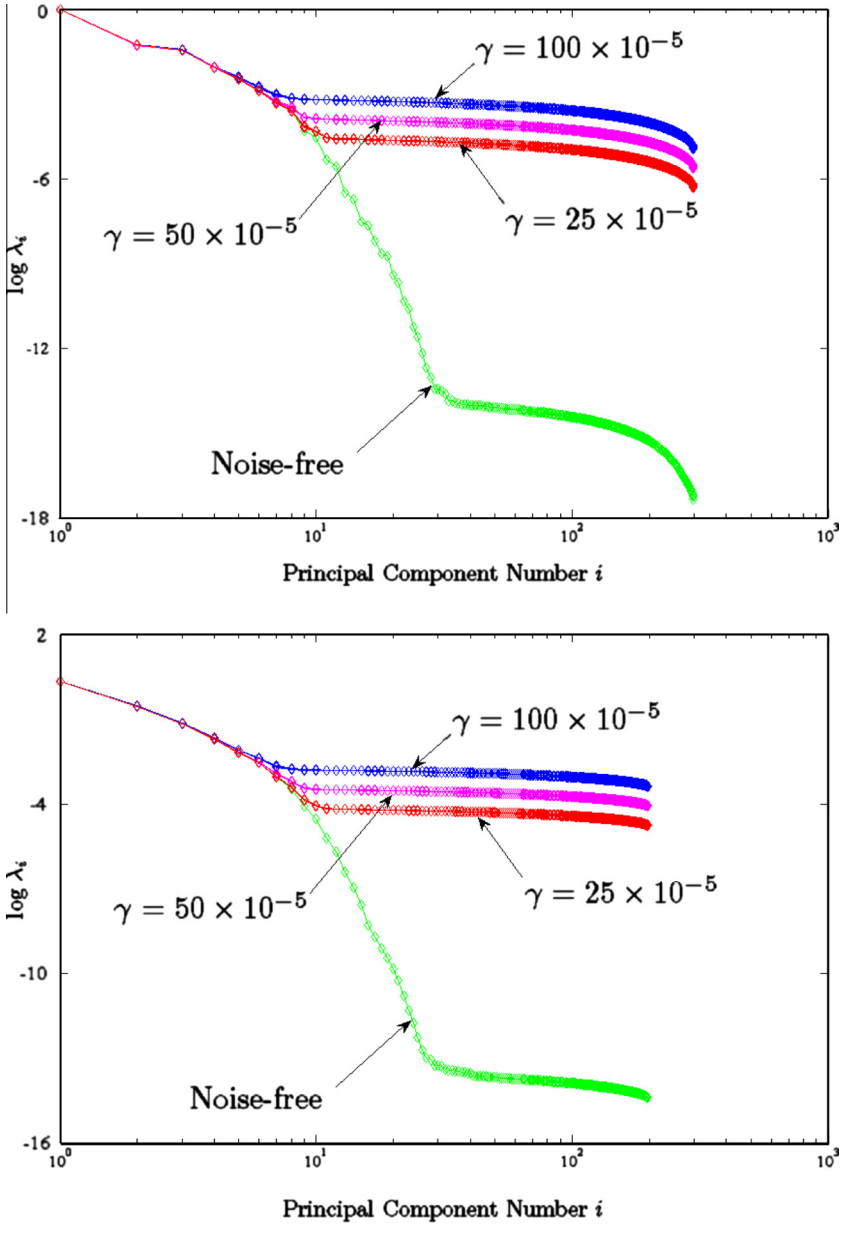

Fig. 9. LSV spectrum of $\mathbf{E}^r$ for sub-domain A (top) and $\mathbf{E}^c$ for sub-domain B (bottom) show a decreasing number of dominant singular values for increasing noise levels.

6. Results

The procedure of the previous sections is implemented with strain matrices obtained from the finite element analysis. Eqs. (22)–(25) are solved for the material parameters and it is seen that the results obtained for Q_{11}, Q_{12}, Q_{22} and Q_{66} are identical to the values input into the finite-element analysis. This agreement with input parameters serves as partial evidence in support of the efficacy of EVFM.

However, a full validation of EVFM must also take into account the effect of noise, which is inevitable in experimental measurements; no significant noise is present in the strain matrices obtained from FEA. To address this issue, we add Gaussian white noise of specified amplitude γ to each of the three finite-element strain matrices and use these as inputs to the EVFM procedure. We follow the method of Pierron and Grediac (2012) and repeat this process for 30 different realizations of noise at 20 equally-spaced γ values in the interval $[5 \times 10^{-5}, 1 \times 10^{-3}]$.

It is observed that for a given value of γ, the LSV spectrum is very repeatable across the 30 realizations. However, as γ increases (Grama and Subramanian, 2013), the LSV spectrum shifts upwards and displays fewer dominant singular values, i.e. those to the left of the point where the curve shows a knee. These trends are readily identifiable in Fig. 9, in which the LSV spectra of $\mathbf{E}^r$ for sub-domain A and $\mathbf{E}^c$ for sub-domain B for various values of γ are shown. At the largest γ value of 1×10^{-3}, only 6 dominant singular values are obtained for $\mathbf{E}^r$ for sub-domain A whereas for the noise-free data, one can identify 28 dominant singular values.

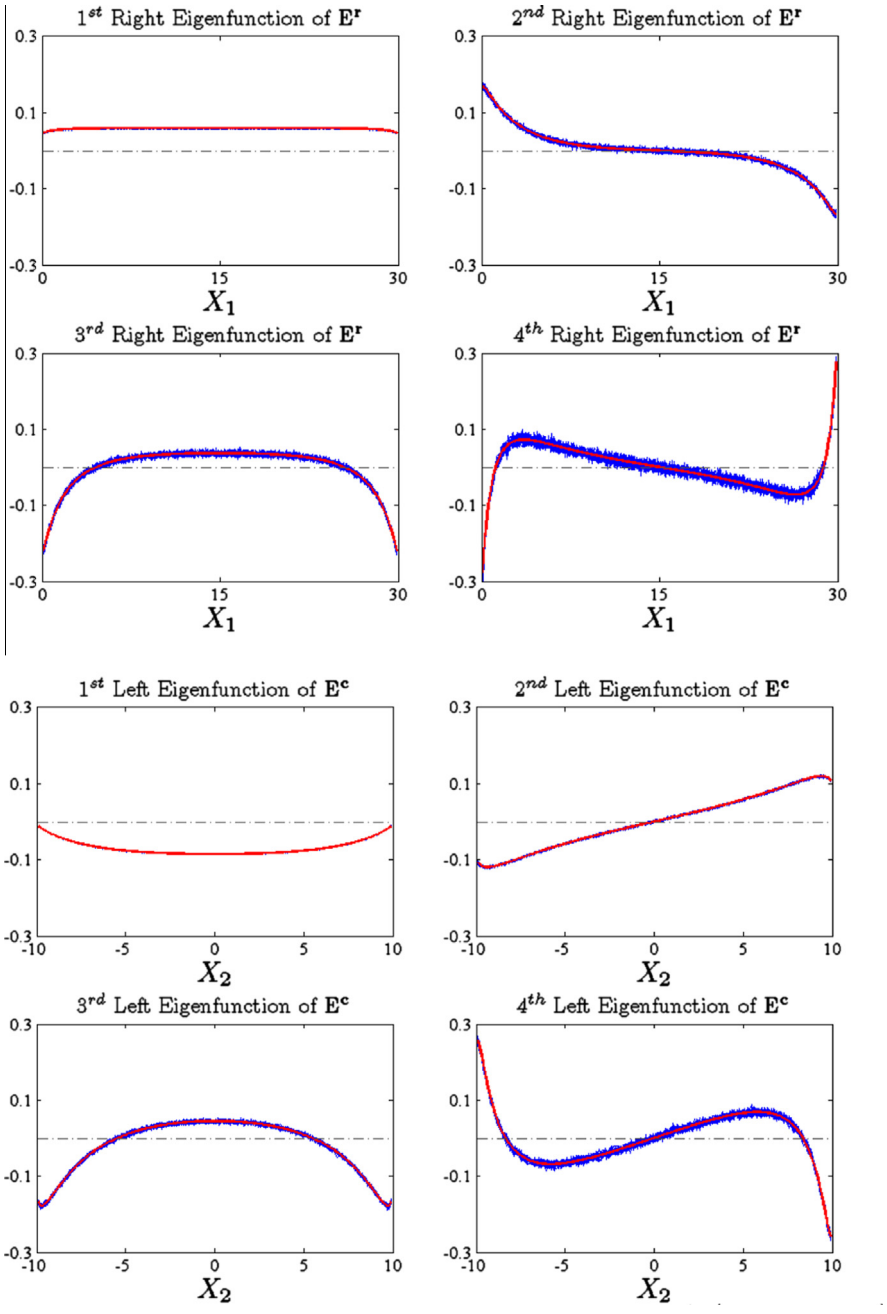

Fig. 10. The first four left eigenfunctions of $\mathbf{E}^r$ for sub-domain A (top two rows) and $\mathbf{E}^c$ of sub-domain B (bottom two rows) for 30 trials, $\gamma = 10^{-3}$ show increasing noise in the eigenfunctions as eigenfunction index increases. In each plot, the blue band is produced by the 30 overlapping noisy eigenfunctions and the red band indicates the corresponding noise-free eigenfunction. (For interpretation of the references to colour in this figure legend, the reader is referred to the web version of this article.)

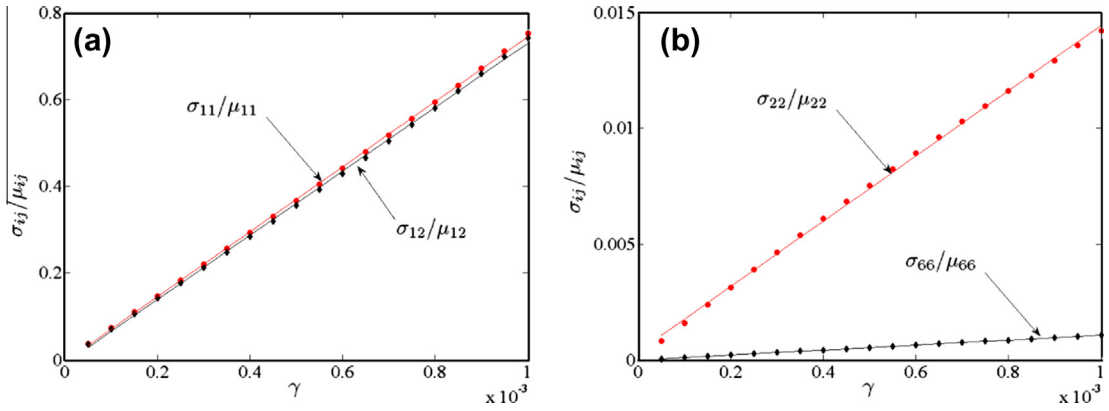

Fig. 11. Coefficients of variation of the four material parameters estimated by the present method. Q_{11} and Q_{22} (left) are much more sensitive to noise than are Q_{12} and Q_{66} (right).

As reported previously in the literature (Grama and Subramanian, 2013), the effect of noise is also evident in the eigenfunctions. As γ increases, each eigenfunction becomes increasingly noisy and the 30 trials produce eigenfunctions that are distributed evenly around the corresponding noise-free eigenfunction. These patterns are evident in the right and left eigenfunctions shown in Fig. 10.

For each repetition at each γ level, the EVFM procedure is executed using the noisy strain matrices as inputs. For each parameter Q_{ij}, the mean value (μ_{ij} and the standard deviation (σ_{ij}) are calculated and the coefficient of variation (CV) for each material parameter is obtained. The CV is a measure of the sensitivity of the identified parameter to input noise (Pierron and Grediac, 2012); the lower the CV value, the less sensitive the parameter is to noise.

Before we compare our results to those published in Chapter 13 of Pierron and Grediac (2012), we note that there appears to be a typographical error in their Fig. 13.10: the ordinate is labelled $\frac{\eta}{Q}$, whereas it should be labelled $\frac{\eta\gamma}{Q}$ or $\frac{\sigma}{Q}$. The CV values for Q_{11}, Q_{12}, Q_{22} and Q_{66} are plotted in Fig. 11. As shown Pierron and Grediac (2012), our results also indicate that the CVs are linear in input noise amplitude γ; moreover, the CVs computed by the present method show much less scatter around the linear fit than the data in Pierron and Grediac (2012). A possible reason for this is the coarse mesh used in the FE analysis in Pierron and Grediac (2012). Similar scatter is noticed in the present study too when a mesh with the same density of elements as in their study is used to obtain the input strain matrices. The parameter Q_{66} is identified most robustly, while Q_{22} is identified with very little error even at $\gamma = 1 \times 10^{-3}$. However, Q_{11} and Q_{12} remain highly sensitive to noise, and yield unacceptable CVs of 0.8 at $\gamma = 1 \times 10^{-3}$.

The CVs for Q_{66} and Q_{22} obtained in the present study are 0.001 and 0.014 respectively, while those in Pierron and Grediac (2012) are 0.004 and 0.084 for the optimized polynomial VFM and 0.004 and 0.093 for the optimized piecewise polynomial VFM respectively. Thus, the present method recovers these parameters more robustly than the optimized polynomial and piecewise polynomial VFM used by Pierron and Grediac (2012). On the other hand, the present study yields CVs of 0.751 and 0.741 for Q_{11} and Q_{12}, while the corresponding values from Pierron and Grediac (2012) are (0.031, 0.186) using piecewise optimized polynomials and (0.030, 0.114) for optimized polynomials, both of which are superior to those obtained in the present study.

7. Discussion

The high CVs for Q_{11} and Q_{12} can be better understood by investigating the four Eqs. (22)–(25). For the 30 repetitions with $\gamma = 1 \times 10^{-3}$, the individual CVs for the 7 coefficients (Eqs. (27)) appearing in these equations are listed in Table 2. Six of the coefficients are seen to have very small CVs, while one, A_{43}, has an anomalously large coefficient. The small CV of A_{14} directly translates to a small CV for Q_{66}, while the small CVs of A_{21} and A_{23} make the ratio $\frac{Q_{11}}{Q_{12}}$ relatively insensitive to noise (CV of 0.093). However, the large CV of A_{43} results in a large CV for Q_{12}, which when coupled with the low CV of $\frac{Q_{11}}{Q_{12}}$, directly leads to a large CV for Q_{11}.

The large CV for A_{43} is not surprising when we look at the effect of noise on the eigenfunctions and the relative magnitude of the strain components. The third eigenfunction is much more noisy when compared to the first eigenfunction (Fig. 10); over the 30 trials, the components of the third eigenfunction display much more variation than do those of the first. Further, ε_1 is the strain component that has the smallest magnitude and therefore will have the largest variance in magnitude for a given magnitude of noise. Considering that A_{43} is obtained by summing up the components of each row of ε_1 along the third eigenfunction, it is then clear as to why this coefficient is the most affected by noise. The effect of the noisy third eigenfunction may also be readily seen by comparing the coefficients A_{32} and A_{42}; both are obtained by using the same strain component, but the former uses the relatively noise-free first eigenfunction while the latter uses the noisy third eigenfunction. This change in eigenfunction is sufficient to increase the CV of the coefficient from 0.0038 to 0.0158.

The present method yields acceptable identification of the material parameters for low to moderate noise, but for large amounts of noise, the procedure has to be improved to be satisfactory. Since the primary reason for the large sensitivity to noise is the sensitivity of the third eigenfunction to noise, a feasible approach is to smooth the third eigenfunction prior to computing the virtual work integrals. Simultaneously, the strain fields may also be reconstructed using smoothed dominant eigenfunctions. Alternatively, different test configurations may be tried out that facilitate more virtual fields using the first dominant eigenfunction,

Table 2
Coefficients of variation of the 7 coefficients appearing in the EVFM equations.

Matrix coefficient	Coefficient of variation
A_{14}	0.0011
A_{21}	0.0908
A_{23}	0.0069
A_{32}	0.0038
A_{33}	0.0613
A_{42}	0.0158
A_{43}	3.9128

and if necessary, the second; both these eigenfunctions are less sensitive to noise and will yield smaller CVs for the material parameters than when using the third.

8. Conclusions

1. In this work, the Eigenfunction Virtual Fields Method has been formulated and applied to the problem of estimation of orthotropic elastic properties from full-field strain data
2. Four virtual fields have been proposed based on eigenfunctions of the composite strain field and a compact system of 4 equations in the 4 unknown material parameters derived and solved.
3. The method yields exact answers for noise-free synthetic strain data, generated using finite-element analysis of the unnotched Iosipescu test.
4. The effect of noise has been studied by adding Gaussian white noise to the synthetic strain data and evaluating the CV of the computed material parameters.
5. It is shown two of the material parameters are less sensitive to noise when computed by the present method than by using the optimized polynomial and optimized piecewise polynomial VFM techniques of Pierron and Grediac (2012). On the other hand, the other two parameters are more severely affected by noise.
6. The high CVs of the material parameters is traced to the pronounced noise in the third dominant eigenfunction and possible future improvements to reduce the sensitivity of these parameters to noise are suggested.

References

Avril, S., Bonnet, M., Bretelle, A.-S., Grédiac, M., Hild, F., Ienny, P., Latourte, F., Lemosse, D., Pagano, S., Pagnacco, E., et al., 2008. Overview of identification methods of mechanical parameters based on full-field measurements. Experimental Mechanics 48 (4), 381–402.

Avril, S., Grediac, M., Pierron, F., 2004. Sensitivity of the Virtual Fields Method to noisy data. Computational Mechanics 34 (6), 439–452.

Avril, S., Pierron, F., 2007. General framework for the identification of constitutive parameters from full-field measurements in linear elasticity. International Journal of Solids and Structures 44, 4978–5002.

Cadima, J., Jolliffe, I., 2009. On relationships between uncentered and column-centered principal component analysis. Pakistan Journal of Statistics 25 (4), 473–503.

Grama, S.N., Subramanian, S.J., 2013. Computation of full-field strains using principal component analysis. Experimental Mechanics. accepted for publication. http://dx.doi.org/10.007/211340-013-9800-z.

Grediac, M., 1989. Principe des travaux virtuels et identification/principle of virtual work and identification. Comptes Rendus de l'Academie des Sciences 309-II, 1–5.

Grediac, M., Pierron, F., Surrel, Y., 1999. Novel procedure for complete in-plane composite characterization using a single T-shaped specimen. Experimental Mechanics 39 (2), 142–149.

Grediac, M., Toussaint, E., Pierron, F., 2002a. Special Virtual Fields for the direct determination of material parameters with the Virtual Fields Method. 1 – Principle and definition. International Journal of Solids and Structures 39, 2691–2705.

Grediac, M., Toussaint, E., Pierron, F., 2002b. Special Virtual Fields for the direct determination of material properties with the Virtual Fields Method. 2 – Application to in-plane properties. International Journal of Solids and Structures 39, 2707–2730.

Jolliffe, I.T., 2002. Principal Component Analysis. Springer.

Malvern, L.E., 1977. Introduction to the Mechanics of a Continuous Medium. Prentice-Hall.

Noy-Meir, I., 1973. Data transformations in ecological ordination: I. some advantages of non-centering. The Journal of Ecology, 329–341.

Pierron, F., Grediac, M., 2000. Identification of the through-thickness moduli of thick composites from whole-field measurements using the Iosipescu fixture: theory and simulations. Composites Part A-Applied Science 31, 309–318.

Pierron, F., Grediac, M., 2012. The Virtual Fields Method: Extracting Constitutive Mechanical Parameters from Full-field Deformation Measurements. Springer.

Pierron, F., Vert, G., Burguete, R., Arvil, S., Rotiant, R., Wisnom, M.R., 2007. Identification of the orthotropic elastic stiffnesses of composites with the Virtual Fields Method: sensitivity study and experimental validation. Strain 43, 250–259.

Strang, G., 2006. Linear Algebra and its Applications. Cengage Learning.

Subramanian, S.J., 2013. The Eigenfunction Virtual Fields Method. Presented at the SEM Annual Congress and Exposition, Lombard, IL, USA.

Toussaint, E., Grediac, M., Pierron, F., 2006. The Virtual Fields Method with piecewise virtual fields. International Journal of Mechanical Sciences 48 (3), 256, 64.